Chemical Science

Accepted Manuscript

This article can be cited before page numbers have been issued, to do this please use: C. Wu, M. Chen, B. Wang, L. Luo, Q. Zhou, G. Mao, Y. Xiong and Q. Wang, *Chem. Sci.*, 2024, DOI: 10.1039/D4SC02824D.

ROYAL SOCIETY OF CHEMISTRY

rsc.li/chemical-science

View Article Online
DOI: 10.1039/D4SC02824D

Data availability

The authors declare that the data are available within the paper and its ESI file.

View Article Online
DOI: 10.1039/D4SC02824D

ARTICLE

Orbital Electron Delocalization of Axial-coordinated Modified FeN_4 and Structurally Ordered PtFe Intermetallic Synergistically for Efficient Oxygen Reduction Reaction Catalysis

Received 00th January 20xx,
Accepted 00th January 20xx

DOI: 10.1039/x0xx00000x

Chenzhong Wu, Meida Chen, Bin Wang, Leqing Luo, Qian Zhou, Guangtao Mao, Yuan Xiong and Qingmei Wang *

Regulating the chemical environment of materials to optimize its electronic structure, leading to the optimal adsorption energies of intermediates, is of paramount importance to improving the performance of electrocatalysis, yet remains an immense challenge. Herein, we design a harmonious axial-coordination Pt_xFe/FeN_4CCl catalyst integrated structurally ordered PtFe intermetallic with orbital electron-delocalization FeN_4CCl support for synergistically efficient oxygen reduction catalysis. The obtained Pt_2Fe/FeN_4CCl with favorable atomic arrangement and surface composition exhibit enhanced oxygen reduction reaction (ORR) intrinsic activity and durability, achieving mass activity (MA) and specific activity (SA) of 1.637 $A{\cdot}mg_{pt}^{-1}$ and 2.270 $mA{\cdot}cm^{-2}$, respectively. Detailed X-ray absorption fine spectroscopy (XAFS) further confirms the axial-coupling effect of FeN_4CCl substrate by configuring the Fe-N bond for ~1.92 Å and Fe-Cl bond for ~2.06 Å. Additionally, Fourier transforms of the extended X-ray absorption fine structure (FT-EXAFS) demonstrate relatively prominent peaks at ~1.5Å, ascribed to the contribution of the Fe-N/Fe-Cl, further indicating the construction of FeN_4CCl moiety structure. More importantly, electron localization function (ELF) and density functional theory (DFT) further determine an orbital electron delocalization effect due to the strong axial traction between Cl atoms and the FeN_4, resulting in electron redistribution and coordination surroundings modification, thus optimizing the adsorption free energy of OH_{abs} intermediates and effectively accelerating ORR catalytic kinetic process.

1. Introduction

Proton exchange membrane fuel cells (PEMFCs) as a potential clean energy-efficient conversion technique have gained numerous attentions owing to their characteristic of environmental-friendly and high-efficiency as power sources for a variety of transportation systems, especially mid-size and heavy-duty vehicles and light railway transits.[1,2] For large-scale applications, a key developmental target for these PEMFCs is to reduce the extensive use of precious platinum in Pt-based nanocatalysts.[3] At present, the consumption of Pt in fuel cell stacks has decreased to 0.3-0.4g_{Pt}/kW, but there is still a considerable gap from the requirements of fuel cell vehicle industrialization (<0.1g_{Pt}/kW).[4,5] For fulfil this purpose, researchers focused on the following: (1) developing a catalyst with optimized coordination circumstances to modify the electron structure of Pt and adsorption energy of intermediates for accelerate the oxygen reduction reaction (ORR) kinetics; (2) designing a catalyst with structurally ordered phase for eliminating dissolution of less-noble metal at the atomic scale observed in disordered counterpart; (3) conceiving a highly stable support for enhance the bond length to resistance the corrosion of carrier and ensure accessibility of sites to maximize Pt utilization.[6-8]

For simultaneously realizing the enhancement of mass activities and stability in fuel cells, great efforts in the development of such advanced Pt-based catalysts have been dedicated.[9,10] Among which, the carbon-supported Pt-based alloy materials have gained tremendous attraction because of the speed ORR kinetics in acidic media, yet they are not still durable enough for practical commercial applications owing to the carbon corrosion in potential cycling.[11,12] The formation of supported structurally ordered Pt-based electrocatalysts with determined atomic arrangement and surface composition that consist of transition metal atomically dispersed in nitrogen-coordinated carbon (M-N-C, M=Fe, Co, Ni, Mn, etc.) support and structurally ordered phase have emerged as promising candidates with improved durability and mass activity towards ORR.[13,14] Unfortunately, the N atom in M-N-C will be attacked by protons generated during the reduction reaction (M-N+H_2O → $M(OH)_2$+$(NH)_2$), leading to the breaking of the M-N bond and the continuous dissolution of metal from the single atom active center of M, seriously affecting the activity of the catalyst.[15,16] Hence, considerable effort has been injected in addressing above problems, with efforts concentrated, in part, on retouching the coordination environment and the chemical composition of M-N-C.[17,18] Previous DFT calculations have

Guizhou University Key Laboratory of Green Chemical and Clean Energy Technology, Guizhou University Engineering Research Center of Efficient Utilization for Industrial Waste, Institute of Dual-carbon and New Energy Technology Innovation and Development of Guizhou Province, School of Chemistry and Chemical Engineering, Guizhou University, Guiyang 550025, China. E-mail: qmwang3@gzu.edu.cn (Q. M. Wang)

† Footnotes relating to the title and/or authors should appear here.

Electronic Supplementary Information (ESI) available: [details of any supplementary information available should be included here]. See DOI: 10.1039/x0xx00000x

proven that the configuration coordination environment of M-N-C can determine the electronic-structure of Pt and M, which remarkedly affects the adsorption free energy of the oxygen species ($O_{2,abs}$, $H_2O_{2,abs}$, OH_{abs} and OOH_{abs}) with the Pt center and thus gives rise to variations in ORR intrinsic activity.[19,20] Thus, in this direction, a catalyst with an optimized coordination state for active Pt sites and a heterogeneous local environment for the M-N-C must be rationally designed and engineered.

Herein, we successfully synthesize a concordant Pt_xFe/FeN_4CCl catalysts that combined the axial-coordinated modified FeN_4 of an orbital electron delocalization effect with structurally ordered PtFe intermetallic for synergistically high-efficient ORR. The unique structure of the catalyst was fabricated by pyrolysis reduction strategy at the high-temperature conditions (**Scheme S1**), in which Fe in the hemin precursor alloying with Pt atoms and formed axial-coordinated modified Fe single-atom. X-ray adsorption fine spectroscopy (XAFS) analyses reveal that a Fe atom coordinates with one axial Cl atom and four N atoms, effectively authenticating the structure of three-dimensional FeN_4CCl architectures. The orbital electron delocalization of chlorine-coordinated modified FeN_4 in FeN_4CCl supports was affirmed by configuring the Fe-N bond for ~1.92 Å and Fe-Cl bond for ~2.06 Å. Additionally, DFT calculations proclaimed that the $PtFe/FeN_4CCl$ shows the lowest adsorption free energy of OH_{abs} species (E_{OHabs}=2.51 eV) relative to FeN_4C (E_{OHabs}=3.07 eV), FeN_4CCl (E_{OHabs}=2.75 eV), and PtFe (E_{OHabs}=3.25 eV). This is attributed to the electron redistribution and coordination surroundings modification, resulting from a strong axial traction effect between Cl atoms and the FeN_4. Benefiting from chlorine-coordinated modified FeN_4CCl support and the synergistic catalysis with the structurally ordered PtFe intermetallic, the obtained Pt_2Fe/FeN_4CCl catalyst with optimum surface composition exhibits a higher MA of 1.637 $A mg_{pt}^{-1}$ and SA of 2.270 mA cm^{-2}, respectively, surpassing the commercial Pt/C catalyst (0.165 A mg_{pt}^{-1} and 0.264 mA cm^{-2}). Therefore, our work gains perspicacious clairvoyance into designing high-performance electrocatalysts with synergistic catalysis by combining tailored to optimize axial-coordinated modified of non-precious metal active sites with a structurally ordered Pt-based intermetallic.

2. Results and discussion

2.1 Morphology and structure characterization

The structures and crystallinity properties of Pt_xFe/FeN_4CCl samples and commercial Pt/C were characterized by powder X-ray diffraction (PXRD), where X represents the weight ratio of Pt to contained Fe in the hemin precursor (X = 1, 2, and 3, respectively, the more detailed particulars in the Supporting Information). All the characteristic diffraction peaks of Pt_xFe/FeN_4CCl sample slightly positive shift to higher angles compared with the commercial Pt/C catalyst (PDF#04-0802), suggesting that the alloy phase has been attained by the introduction of smaller Fe atoms (**Figure 1a**).[21] Importantly, the ordered characteristic peaks at 2θ of 23.93° for the (001) plane, 33.90° for the (110) plane, and 41.07° for the (111) plane were further observed in Pt_xFe/FeN_4CCl sample, indicating the formation of structurally ordered PtFe intermetallic (PDF#43-1359).[22,23] In addition, the ordered degree of all as-prepared catalysts was determined by calculating the peak intensity ratio of the characteristic planes (110) and (111), which demonstrated that the Pt_2Fe/FeN_4CCl (0.275) shows a higher ordered degree than that of Pt_1Fe/FeN_4CCl (0.233) and Pt_3Fe/FeN_4CCl (0.266) (**Table S1**).[24,25] The Pt_2Fe/FeN_4CCl catalyst with a higher ordered degree and favorable surface composition was synthesized by precisely manipulating the feeding weight ratio of Pt to the contained Fe^{2+} precursor. The shape and structure of as-prepared Pt_2Fe/FeN_4CCl materials were further investigated by transmission electron microscopy (TEM), aberration-corrected high-angle annular dark field scanning transmission electron microscope (AC-HAADF-STEM), and X-ray energy dispersive spectroscopy (EDS). The overall TEM images of the Pt_2Fe/FN_4CCl and their corresponding particle diameter histograms were presented in **Figure 1b** and **1c**, exhibiting nanoparticles uniformly distributed in the whole support, averaging size of 3.38 ± 0.2 nm in the edge length. The AC-HAADF-STEM analyses were performed to further characterize catalyst structure and surface composition. As displayed in **Figure 1d**, we can observe that abundant bright isolated dots are regularly scattered in the modified graphitic carbon matrix, which is attributed to Fe single atoms, indicating that the Fe single sites co-coordinated with chlorine-nitrogen and embedded in carbon (Fe-N-C-Cl) were formed. Besides, as presented in **Figure 1e-h**, the high-resolution TEM images of Pt_2Fe/FeN_4CCl sample reveal that the as-prepare catalyst nanoparticles composition of ordered PtFe alloy phase and Fe single atoms substrate, further verified that a multiple-structure catalyst has been triumphantly synthesized. The corresponding fast Fourier transform (FFT) further measures lattice fringes with d-spacings of 0.183 nm for the characteristic planes (110) facet and 0.227 nm for the (111) facet, which is consistent with the XRD results. Meanwhile, the corresponding line scan profiles analysis of the area of line 1 and line 2 displayed the formation of ordered PtFe intermetallic via the incorporation of smaller Fe atoms into Pt crystal lattice.[26] Moreover, as shown in **Figure 1i**, EDS element mapping images of Pt_2Fe/FeN_4CCl indicate that Pt atoms are primarily centralized on the whole ordered PtFe intermetallic. However, partial Fe atoms manufacture the ordered intermetallic and another ones are allocated to generate single-atom, demonstrating that the synergistic catalyst consists of ordered PtFe intermetallic and Fe single-atoms support. Furthermore, the atomic ratio of Pt/Fe is estimated as 32/68, confirmed by electron energy loss spectroscopy (EELS) (**Figure 1j**), EDS spectrum (**Figure 1k**), and inductively coupled plasma optical emission spectrometry (ICP-OES) analysis (**Table S2**). Simultaneously, the element of Cl was also detected in the Pt_2Fe/FeN_4CCl catalyst, indicating that the Cl atoms of the hemin precursor have been successfully transformed into axial-ligand of coordinated modified FeN_4CCl substrate.

X-ray adsorption fine spectroscopy (XAFS) analysis was carried out to further analyze the local coordination environment and electronic structure at the atomic level. The Pt L_3-edge X-ray absorption near-edge structure (XANES) spectra of Pt_2Fe/FeN_4CCl with Pt foil and PtO_2 as references are shown in **Figure 2a**.[27] The XANES of white line intensity (~11,569 eV), edge energy, and shapes in Pt_2Fe/FeN_4CCl catalyst are similar to that of Pt foil, suggesting the chemical states are approximately zero-valence. Previous studies have proven that a higher content of Pt (0) in alloy catalysts is beneficial to improving ORR catalytic kinetics.[28] Additionally, the Fourier transforms of the extended X-ray absorption fine structure (FT-EXAFS) spectra (**Figure 2b**) demonstrate that the relatively

View Article Online
DOI: 10.1039/D4SC02824D

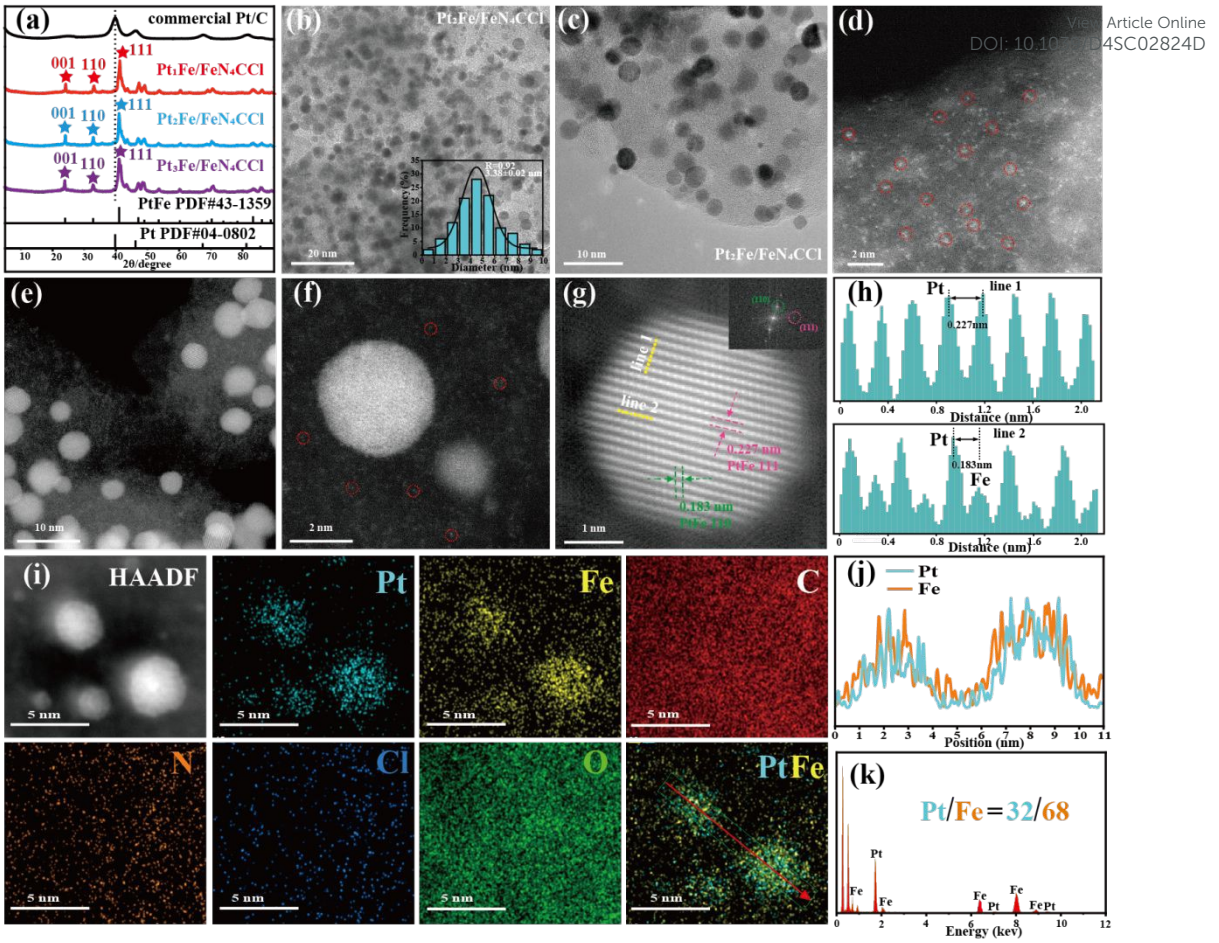

Figure 1. (a) XRD patterns of the commercial Pt/C, Pt_1Fe/FeN_4CCl, Pt_2Fe/FeN_4CCl, and Pt_3Fe/FeN_4CCl sample. (b-c) TEM and the corresponding particle size distribution images of Pt_2Fe/FeN_4CCl. (d-e) AC-HAADF-TEM images of the Pt_2Fe/FeN_4CCl sample and single particle. (f-g) HR-TEM and the corresponding FFT images in the Pt_2Fe/FeN_4CCl sample and (h) the corresponding line scan profiles marked in g, corresponding with the area of line 1 (top) showing only Pt atoms as well as line 2 between Pt and Fe atoms (bottom). (i) HAADF-STEM images of Pt_2Fe/FeN_4CCl sample and corresponding elemental mapping image. (j) EELS profile. (k) EDS spectrum of corresponding element mapping.

prominent peak at ~1.5Å should be assigned to Pt-N bonds, declaring the strong metal-support interaction. [29,30] Moreover, due to heteroatomic interactions in Pt-Fe alloying, a shorter radial distance in comparison to that of Pt foil is ascribed to the contribution of the Pt-Pt/Pt-Fe bond at ~2.63 Å, further indicating the construction of PtFe intermetallic interface.[31] Compared with the R, k and q space diagrams of Pt foil and PtO_2 (**Figure S1**), the fitting information presented in **Figure 2c** by Pt_2Fe/FeN_4CCl further supports that the Pt-Pt bond length is shortened to induce a compressive effect due to the PtFe alloy formation. The scattering peak at ~1.5 Å is from the contribution of Pt-N bonds, suggesting the strong mental-support interaction between PtFe intermetallic and the FeN_4CCl support. In addition, the fitting results of the EXAFS curve also reveal that the coordination number is approximately 6.25 for the Pt-Pt shell, approximately 4.14 for the Pt-Fe shell and approximately 1.46 for the Pt-N shell. The optimized coordination environment and compressive strains described above enhance the catalytic activity of the ORR. (**Figure S2** and **Table S3**). The wavelet transform EXAFS spectroscopy could afford resolution in both radial distance and k-space. Incidentally, the scattering peak at ~2.05 Å more likely assigned to the Ramsauer-Townsend effect, which is caused by the quantum effect rather than the superposition of the sine function because of the existence of heavy-metal elements. The Pt L_3-edge WT contour plots in Pt_2Fe/FeN_4CCl catalyst show that intensity maximum color with Pt-Pt/Pt-Fe bonds at ~9.5 $Å^{-1}$ are shifted upwards compared to Pt foil and PtO_2 (**Figure 2d** and **Figure S3**).[32,33] Meanwhile, the XANES characterization in Pt_2Fe/FeN_4CCl catalyst and Fe foil, FeO, and phthalocyanine (FePc) are shown in **Figure 2e**. The white line intensity of the Fe K-edge in Pt_2Fe/FeN_4CCl (~7122 eV) is located among Fe foil and FePc, indicating that the chemical state of Fe species in Pt_2Fe/FeN_4CCl samples is probably concentrated on metal Fe and oxidated Fe. Moreover, FT-EXAFS at the Fe K-edge presents primary peaks at ~1.5 Å, ~2.09 Å and ~2.72 Å, which are reasonably in line with the scattering paths of Fe-N/Fe-Cl,[34,35] Fe-Fe,[36] and Fe-Pt,[37] respectively (**Figure 2f**). It is worth noting that the scattering paths Fe-N at ~1.5 Å probably offer evidence for the existence of the square-planar Fe-N_4 configuration with a porphyrin-like structure.[38,39] As a verification, the coordination configuration of Fe atoms was analyzed by quantitatively fitting the EXAFS spectra. As shown in **Figure 2g**, the fitted structural parameters suggest that a Fe atom is coordinated with one axial Cl atom at ~2.06 Å and four N atoms at ~1.92 Å, individually (**Figure S4** and **Table S4**), substantiating

View Article Online
DOI: 10.1039/D4SC02824D

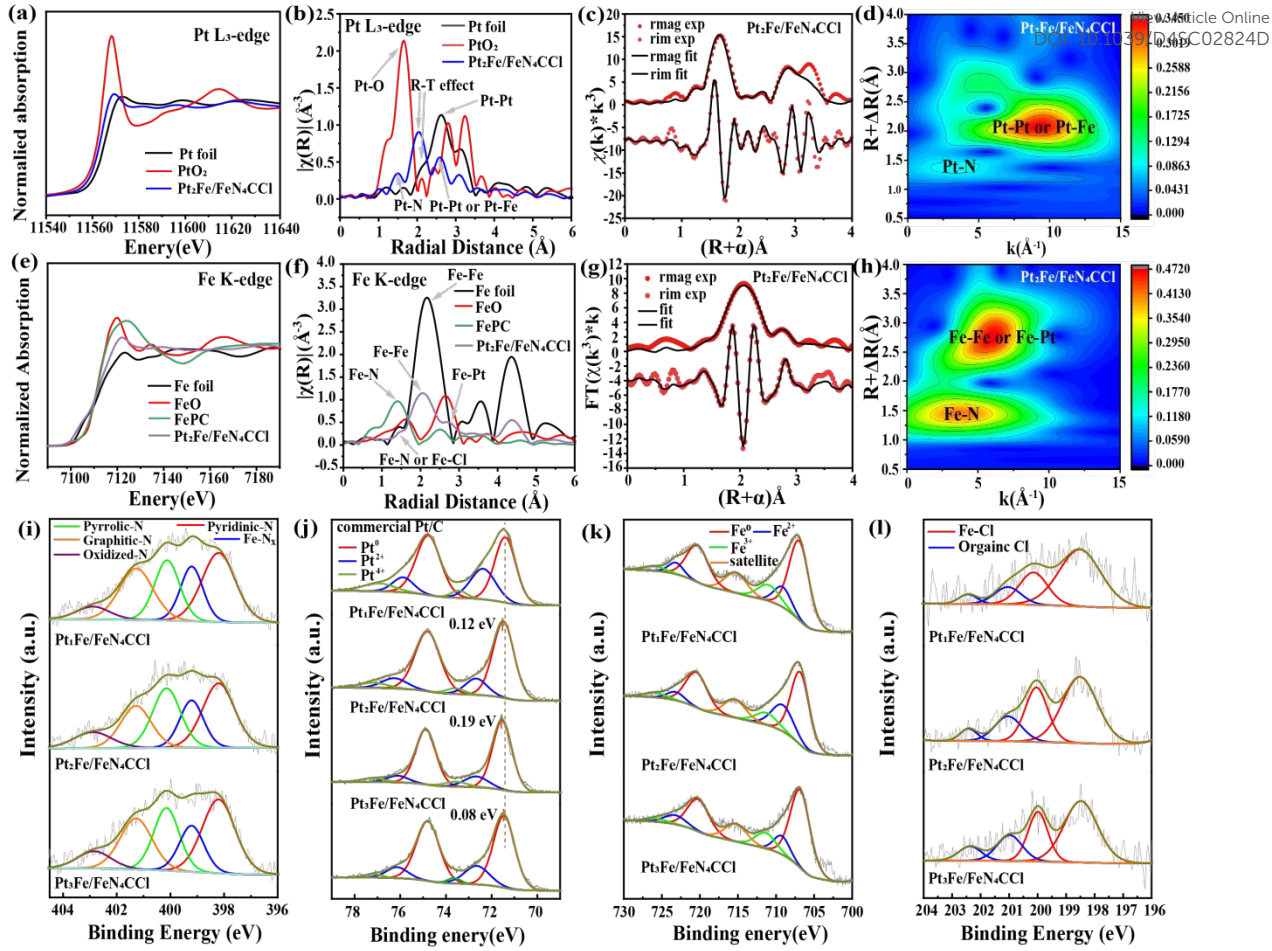

Figure 2. (a-c) XAFS diagram of Pt L_3-edge XANES for Pt foil, PtO_2 and Pt_2Fe/FeN_4CCl (a), the Fourier transforms of EXAFS spectra for Pt foil, PtO_2 and Pt_2Fe/FeN_4CCl (b), the EXAFS fitting curve Pt L_3-edge of Pt_2Fe/FeN_4CCl catalyst at R-space (c) and wavelet transform of the Pt L_3-edge of corresponding EXAFS spectra for Pt_2Fe/FeN_4CCl catalyst (d). (e-h) XAFS diagram of Fe K-edge XANES for Fe foil, FeO, FePc and Pt_2Fe/FeN_4CCl (e), the Fourier transforms of EXAFS spectra for Fe foil, FeO, FePc and Pt_2Fe/FeN_4CCl (f), the EXAFS fitting curve Fe K-edge of Pt_2Fe/FeN_4CCl catalyst at R-space(g) and wavelet transform of the Fe K-edge of corresponding EXAFS spectra for Pt_2Fe/FeN_4CCl catalyst (h). (i-l) XPS spectra of N 1s (i), Pt 4f (j), Fe 2p (k) and Cl 2p (l).

that the three-dimensional FeN_4CCl architectures was attained (**Figure S5**). The fitting scattering path information of benchmarked against Fe foil, FeO and FePc was plotted in **Figure S6**. The Fe K-edge WT contour plots of Pt_2Fe/FeN_4CCl catalyst signify that the intensity maximum ~4 $Å^{-1}$ for Fe-N/Fe-Cl and ~6.1 $Å^{-1}$ for FeFe/Fe-Pt and similar with the wavelet-transform contour plots of Fe foil, FeO and FePc, respectively (**Figure 2h** and **Figure S7**).[40,41] These combined results further confirm the successful construction of FeN_4CCl moieties, optimized axial-coordinated effect and suitable electronic interface for intermediate adsorption and desorption.

X-ray photoelectron spectroscopy (XPS) further examined the surface chemical composition and electronic valence state of as-prepared catalyst. The presence of Pt, Fe, Cl, N, C, and O elements are confirmed by the XPS survey of the Pt_xFe/FeN_4CCl sample (**Figure S8** and **Table S5**), which is consistent with the EDS profiles. The fitted peak of C1s contains C-N peaks compared with commercial Pt/C catalyst, indicating presumable nitrogen-dope in the as-prepared catalyst support (**Figure S9** and **Table S6**). Notably, the fitted peak of characteristic N 1s spectra contains Fe-N_x peaks, further identifying the occurrence of FeN_4 sites, which matched with XAFS analysis results (**Figure 2i** and **Table S7**).[42] Based on the peak fitting of the Pt 4f (**Figure 2j, Figure S10a** and **Table S8**), the Pt (0) mainly concentrates on the chemical state of metal in commercial Pt/C, Pt_1Fe/FeN_4CCl, Pt_2Fe/FeN_4CCl, Pt_2Fe/FeN_4CCl and ordered PtFe NPs catalyst, benefiting for accelerating the entire ORR circle.[43] Importantly, compared with the standard Pt 4f of Pt/C, the electron density of Pt (positive shift +0.12eV for Pt_1Fe/FeN_4CCl, +0.19eV for Pt_2Fe/FeN_4CCl, +0.08eV for Pt_3Fe/FeN_4CCl and negative shift -0.11eV for ordered PtFe NPs, respectively) indicates the strong interactions between PtFe and FeN_4CCl.[44] However, the Pt_2Fe/FeN_4CCl catalyst was modified with FeN_4CCl support, which drew plenty of electrons due to the strong electronegativity of Cl ligands (3.16), thus resulting in a positive binding energy shift. Furthermore, a negative binding energy shift was exhibited for Fe 2p on Pt_2Fe/FeN_4CCl (-0.26 eV) as compared to the FeN_4C SACs at 707.03 eV, demonstrating that the axial-coordinated traction effect of Cl ligands regulates electron structure (**Figure 2k, Figure S10b** and **Table S9**). Meanwhile, the Fe 2p of ordered PtFe NPs (0.14 eV) suggests a positive binding energy shift compared with the Pt_2Fe/FeN_4CCl at 706.77 eV, in line with Pt 4f results. Noticed, combined with the Cl 2p characteristic spectrum, the Cl species mainly exist in

View Article Online
DOI: 10.1039/D4SC02824D

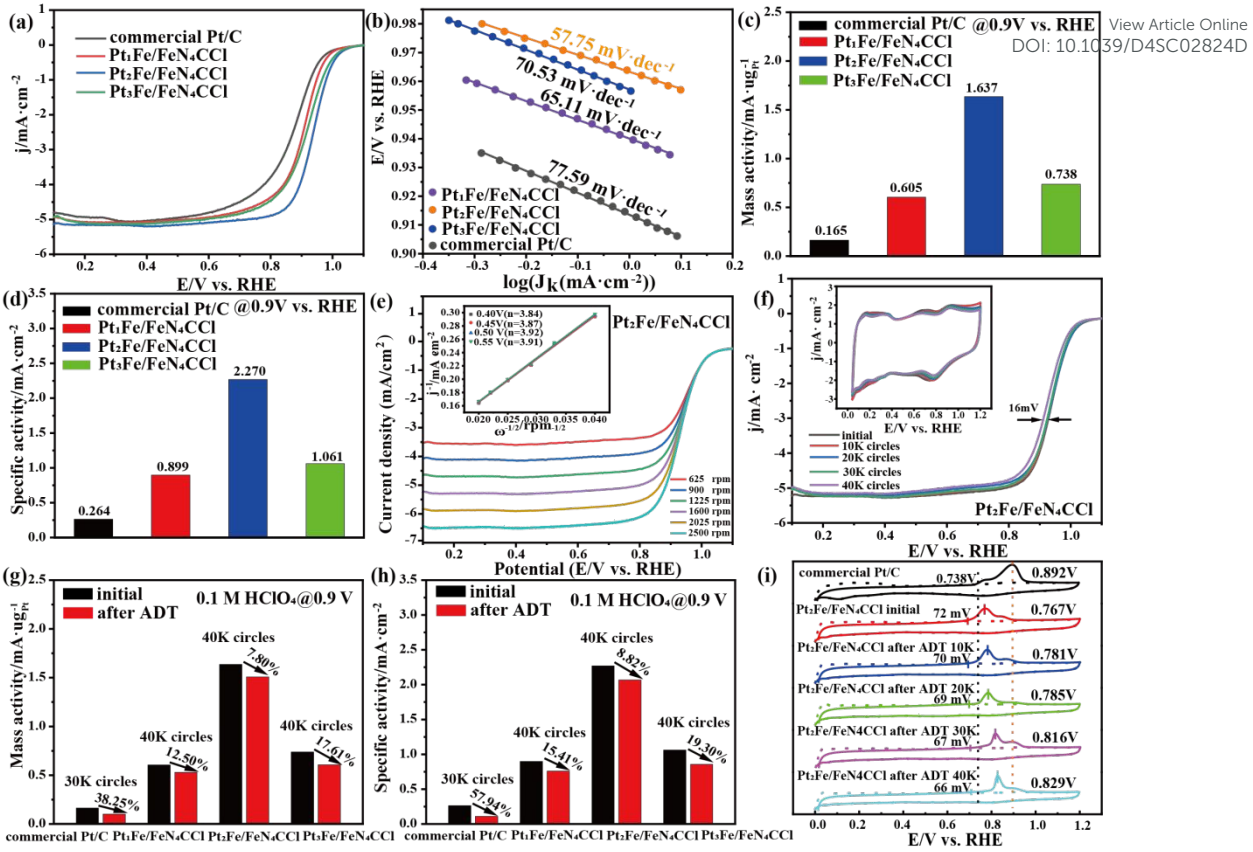

Figure 3. (a) LSV curves of Pt_1Fe/FeN_4CCl, Pt_2Fe/FeN_4CCl, Pt_3Fe/FeN_4CCl, and commercial Pt/C catalysts in O_2-saturated 0.1 M $HClO_4$ solution, sweep rate 10 mV/s, and rotation rate 1600 rpm. (b) the Tafel plots of Pt_1Fe/FeN_4CCl, Pt_2Fe/FeN_4CCl, Pt_3Fe/FeN_4CCl, and commercial Pt/C catalysts. (c-d) the MA and SA of Pt_1Fe/FeN_4CCl, Pt_2Fe/FeN_4CCl, Pt_3Fe/FeN_4CCl, and commercial Pt/C catalysts. (e) ORR polarization curves of Pt_2Fe/FeN_4CCl catalysts at various rotation rates and Koutecky-Levich plots at various electrode potentials. (f) ORR polarization curves of Pt_2Fe/FeN_4CCl catalysts before and after 40,000 sweeping cycles (inset is the CV curves of Pt_2Fe/FeN_4CCl). (g-h) the changes of MA and SA of Pt_1Fe/FeN_4CCl, Pt_2Fe/FeN_4CCl, Pt_3Fe/FeN_4CCl, and commercial Pt/C catalysts before and after ADT in different circles. (i) CO stripping voltammetry in 0.1 M $HClO_4$ electrolyte of Pt_2Fe/FeN_4CCl catalyst compared with commercial Pt/C.

the form of Fe-Cl coordination (**Figure 2l** and **Table S10**), suggesting the Cl atoms axial-coordinated with the FeN_4 site, benefiting the adsorption/desorption conversion process.

2.2 ORR performance of the Pt_xFe/FeN_4CCl system

The primary ORR activity of FeN_4C SACs, Pt_1Fe/FeN_4CCl, Pt_2Fe/FeN_4CCl, Pt_3Fe/FeN_4CCl ordered PtFe NPs and commercial Pt/C catalysts was investigated by cyclic voltammetry (CV) and linear sweep voltammetry (LSV) in N_2- and O_2- saturated $HClO_4$ solutions, respectively. As shown in **Figure S11a and S11b**, the CV curves show that the hydrogen adsorption/desorption peaks appear in the region of 0-0.4 V and Pt oxidation/reduction peaks in 0.6-1.2 V, respectively. Moreover, as shown in **Figure 3a and Figure S11c**, the Pt_2Fe/FeN_4CCl shows a higher ORR activity with a half-wave potential ($E_{1/2}$) of 0.936V vs. reversible hydrogen electrode (RHE) relative to FeN_4C SACs (0.851 V), Pt_1Fe/FeN_4CCl (0.909 V), Pt_3Fe/FeN_4CCl (0.920 V), ordered PtFe NPs (0.903 V) and commercial Pt/C (0.876 V) catalysts. The Tafel slope as a significant kinetic parameter is displayed in **Figure 3b and Figure 11d**. The value of the Tafel slope for Pt_2Fe/FeN_4CCl (57.75 $mV \cdot dec^{-1}$) sample is lower than that of the FeN_4C SACs (117.24 $mV \cdot dec^{-1}$), Pt_1Fe/FeN_4CCl (65.11 $mV \cdot dec^{-1}$), Pt_3Fe/FeN_4CCl (70.53 $mV \cdot dec^{-1}$), ordered PtFe NPs (72.35.35 $mV \cdot dec^{-1}$) and commercial Pt/C (77.59 $mV \cdot dec^{-1}$) counterparts, indicating the more higher ORR kinetics of Pt_2Fe/FeN_4CCl ones. The electrochemical surface area (ECSA) was measured to further evaluate the ORR intrinsic activity by the CO-stripping experiments, instead of hydrogen underpotential deposition (HUPD), considering the suppression of H_{upd} adsorption on Pt-M alloy catalysts.[45] The mass activity (MA) and specific activity (SA) at 0.9 V vs RHE of all catalysts were calculated by normalizing the Pt loading and ECSA (**Table S11**). As shown in **Figure 3c, d and Figure S11e**, the MA/SA of Pt_2Fe/FeN_4CCl was 1.637 $A \cdot mg_{Pt}^{-1}$/2.270 $mA \cdot cm^{-2}$, which is about 2.71/2.53, 2.22/2.14, 3.13/2.66 and 9.92/8.60 times higher than that of Pt_1Fe/FeN_4CCl (0.605 $A \cdot mg_{Pt}^{-1}$/0.899 $mA \cdot cm^{-2}$), Pt_3Fe/FeN_4CCl (0.738 $A \cdot mg_{Pt}^{-1}$/1.061 $mA \cdot cm^{-2}$), ordered PtFe NPs (0.523 $A \cdot mg_{Pt}^{-1}$/0.852 $mA \cdot cm^{-2}$) and commercial Pt/C (0.165 $A \cdot mg_{Pt}^{-1}$/0.264 $mA \cdot cm^{-2}$), respectively. For FeN_4C SACs, the ORR activity was further evaluated by half-wave potential and the kinetic current density (j_K), indicating all as-prepared Pt-based catalyst exhibited superior ORR performance (**Figure S11f**). In addition, **Figure 3e** and **Figure S12** show that the average electron transfer number (n) was calculated at 3.89 for Pt_2Fe/FeN_4CCl, 3.85 for Pt_1Fe/FeN_4CCl, 3.83 for Pt_3Fe/FeN_4CCl and 3.71 for commercial Pt/C by Koutecky-Levich (K-L) equation, demonstrating the unabridged four-electron ($4e^-$) ORR pathway with the reduction of O_2 to H_2O directly.[46] The stability of the

View Article Online
DOI: 10.1039/D4SC02824D

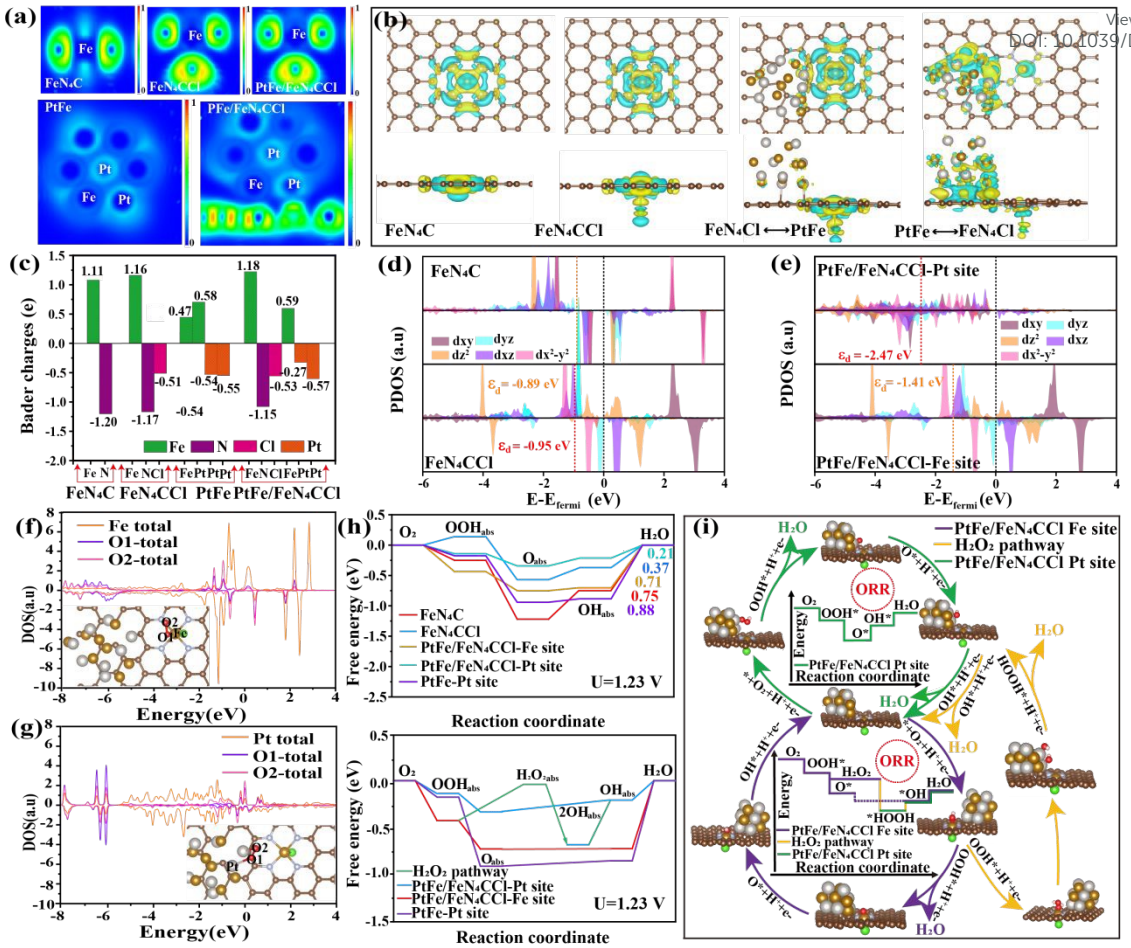

Figure 4. (a) ELF of the center Fe site (the top obtains FeN_4C, FeN_4CCl, and $PtFe/FeN_4CCl$) and the center Pt site (the bottom obtains PtFe and $PtFe/FeN_4CCl$). Scale bars, 0-1. (b) Top and side views of 3D charge density differences for FeN_4C, FeN_4CCl, FeN_4CCl↔PtFe and PtF↔eFeN_4CCl, respectively. (c) The value of transferred Bader Charges of FeN_4C, FeN_4CCl, PtFe, and $PtFe/FeN_4CCl$ at Metal site (Fe and Pt) and surrounding atomic in corresponding structural models. (d) PDOS of Fe-3d in FeN_4C and FeN_4CCl. (e) PDOS of Fe and Pt site in $PtFe/FeN_4CCl$, respectively. (f-g) After the $PtFe/FeN_4CCl$ system interacts with O_2, DOS diagram of the adsorption Metal site (Fe and Pt) with O1 and O2, respectively. (h) (top) Free energy diagrams of different ORR intermediates at 1.23 V and (bottom) ORR catalytic process involved in H_2O_2 intermediate over $PtFe/FeN_4CCl$-Pt site, PtFe-Pt site as well as $PtFe/FeN_4CCl$-Fe site, FeN_4C, FeN_4CCl. (i) Scheme of the pathway in ORR circle of $PtFe/FeN_4CCl$ based on DFT.

as-prepared catalysts and commercial Pt/C for ORR was investigated via an accelerated durability test (ADT) in O_2-saturated 0.1 M $HClO_4$ solution. **Figure S13** displays a larger negative shift (49 mV) of $E_{1/2}$ for commercial Pt/C before and after 30,000 potential cycles. Further, the calculated MA and SA of commercial Pt/C seriously decreased for 38.25 % and 57.94 % relative to original values, respectively. By contrast, the as-prepared Pt_xFe/FeN_4CCl catalyst exhibited enhanced ORR performance (**Table S12**). The Pt_2Fe/FeN_4CCl sample acquired more favourable retention of catalytic activity (only 16 mV negative shift of $E_{1/2}$) after 40,000 sweeping cycles (**Figure 3f**) and afforded a slight loss of 7.80 % in MA and 8.82 % in SA (**Figure 3g, h**). Meanwhile, the LSV curves of as-prepared Pt_1Fe/FeN_4CCl and the Pt_3Fe/FeN_4CCl catalyst exhibit 21 mV and 24 mV negative shift of $E_{1/2}$ before and after 40000 cycles (**Figure S14**), along with accompanying by exiguous drops of 12.50 % and 17.61 % for Pt_1Fe/FeN_4CCl as well as 15.41 % and 19.30 % for Pt_3Fe/FeN_4CCl in MA and SA, respectively. Moreover, the ORR performance of the as-prepared Pt_2Fe/FeN_4CCl catalyst with optimum surface composition is superior to the reported literature (**Table S13**).

To further verify the morphology after ADT, the CO stripping experiments of Pt_1Fe/FeN_4CCl, Pt_2Fe/FeN_4CCl, Pt_3Fe/FeN_4CCl and commercial Pt/C were shown in **Figure 3i** and **Figure S15**. The onset potential of CO oxidation peak of all as-prepared catalysts is much lower than that of commercial Pt/C and fractionally deviated before and after 40,000 CV cycles, indicating the maintenance of the electronic structure and surface composition.[47] Such results demonstrate that the enhanced ORR activity and stability of the as-prepared Pt_xFe/FeN_4CCl catalyst was attributed to the construction of FeN_4CCl moiety with optimized orbital electron-delocalization, formation of ordered phase with definite atomic distribution, surface composition and the strong interaction between PtFe intermetallic and FeN_4CCl substrate.

2.3 Density functional theory computational analysis

Density functional theory (DFT) was carried out to clarify the influence of $PtFe/FeN_4CCl$ structure on the ORR catalytic process. The constructed structural model (after optimization) of FeN_4C, FeN_4CCl, PtFe and $PtFe/FeN_4CCl$, based on the

View Article Online
DOI: 10.1039/D4SC02824D

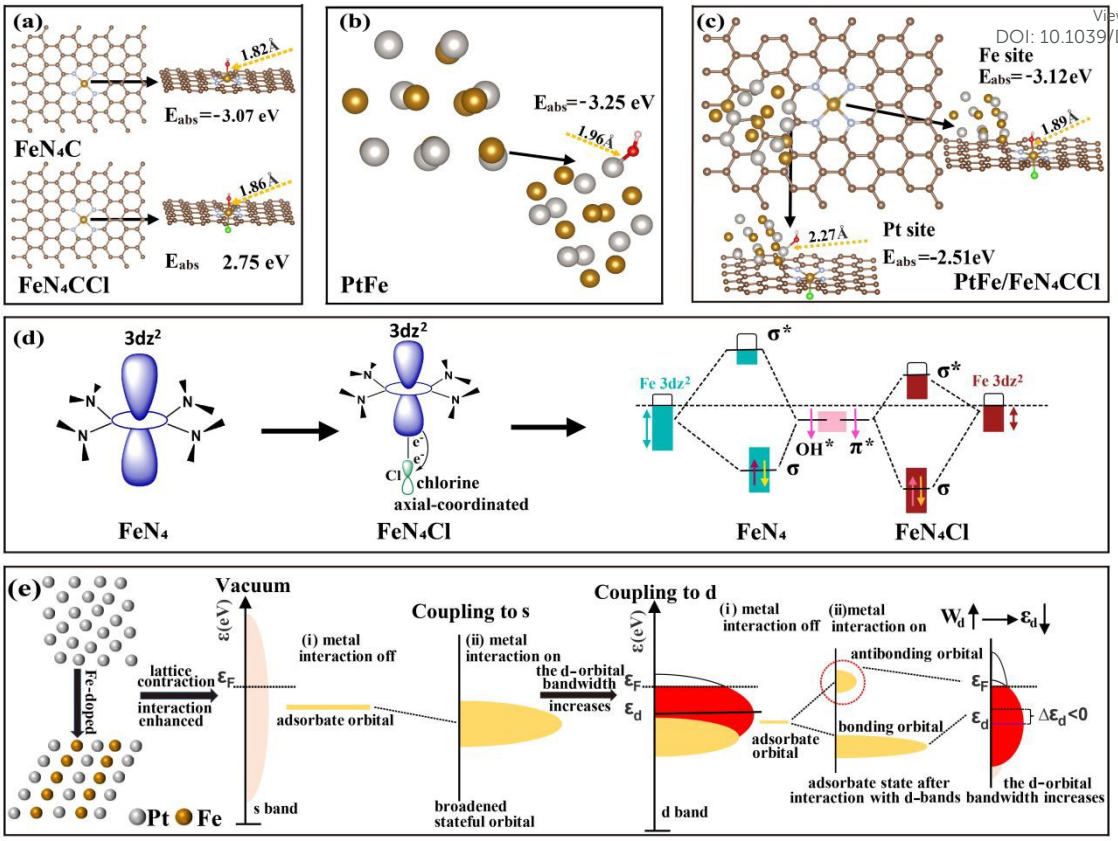

Figure 5. (a-c) The bond lengths and corresponding adsorption free energy with oxygen intermediate on active sites (Fe and Pt). (d) The axial-coordinated Cl atoms lead to an orbital electron delocalization effect of Fe 3d orbitals. (e) The schematic diagram of alloying Pt with a non-precious Fe element, which can exhibit a lattice contraction compared with pure Pt. The alteration of the d-band center could affect its absorption capability of oxygen containing intermediates.

AC-HAADF-TEM images, XAFS and their fitting results, XPS signal analysis, are shown in **Figure S16**. **Figure 4a** and **Figure S17** exhibited the two-dimensional electron localization function (2D ELF) of FeN_4 part in FeN_4C, FeN_4CCl and PtFe/FeN_4CCl as well as PtFe part in PtFe/FeN_4CCl, in which FeN_4 part possesses symmetrical electron localization distribution. The bright region on the Fe site of FeN_4CCl and PtFe/FeN_4CCl becomes darker compared to FeN_4C, testifying that the orbital electron delocalization effect exists induced by the axial-coordinated traction of Cl atoms.[48,49] In comparison, the around color of Pt atoms is brighter compared to the Fe atoms on PtFe part, which is caused significant charge polarization by the electron delocalization degree of both Pt and Fe atoms with different electronegativity.[50] A similar conclusion is drawn from the differential spin density distribution (**Figure S18**). **Figure 4b** displays the charge densities difference (CDD) of FeN_4C, FeN_4CCl, FeN_4CCl-PtFe, and PtFe-FeN_4CCl, which the metal site evidently confirms an inclination to bereft electrons. There appear extremely palpable charge separation/transfer effects around PtFe intermetallic and the FeN_4CCl substrate, exemplifying itsinteraction with the supports and accordingly benefiting for the first adsorption of O_2 in conjunction with the following four-electron steps process. More precisely, compared with FeN_4C and Fe_4CCl, the FeN_4CCl substrate in PtFe/FeN_4CCl catalyst can absorb a significant number of electrons from PtFe intermetallic and form a remarkable positive charge area due to the occurrence of the axial-coordinated Cl atoms. Previous researches have manifested that electron deficiency (or positive-charged) metal sites are instrumental in attenuating the adsorption free energy of OH_{abs} intermediates.[51] Bader charge quantifiable analysis in **Figure 4c** and **Figure S19** further confirms this viewpoint. When Cl atom axial-coordinated modified FeN_4 site, the Fe center transferred electrons of both PtFe/FeN_4CCl (1.18 |e|) and FeN_4CCl (1.16 |e|) is clearly more than in FeN_4C (1.11 |e|). Consistently, while the ordered PtFe nanoparticles embedded into atomically dispersed chlorine-nitrogen-doped Fe single-atoms support, the Pt center in PtFe/FeN_4CCl catalyst of charge accumulation less than that of PtFe without modified Cl atom. These numerical results attest that the axial-coordinated Cl atoms can regulate the electronic structure of the active site, in line with the observation of the above CDD data.[71,72] The effect of axial-coordinated Cl atoms on the electron distribution was further conducted by the partial density of states (PDOS) calculations. As shown in **Figure 4d, e** and **Figure S20**, the d-band center of Fe-3d in FeN_4CCl and PtFe/FeN_4CCl (-0.95 eV and -1.41 eV) shifts down in comparison to FeN_4C (-0.89 eV). The PtFe/FeN_4CCl (-2.47 eV) exhibits a downshifted d-band center compared with PtFe (-2.33 eV). It is evidently demonstrated that the axial-coordinated Cl atoms arouse Fe center electron transfer, inducing the occupancy of orbital electron delocalization,[54,55] which is consistent with the calculated magnetic moment (**Table S14**) and spin density distribution.

To further verify the synergistic ORR catalysis mechanism, we calculated the density of states (DOS) of active site and O_2 molecule to perceive the activation mechanism of $O_{2,abs}$.

According to the molecular orbital theory, the DOS of both O1 and O2 atoms in O_2 molecule is entirely symmetric (**Figure S21**).[56] When O_2 molecule adsorbed on the Fe sites in PtFe/FeN_4CCl (**Figure 4f** and **Figure S22a, b**), FeN_4C (**Figure S23a-c**), and FeN_4CCl (**Figure S23d-f**), the DOS show the significant discrete of the Fe 3d and O 2p orbital state. In contrast, when O_2 molecule adsorb on the Pt sites in both PtFe/FeN_4CCl (**Figure 4g** and **Figure S22c, d**) and PtFe (**Figure S23g-i**), the DOS show a symmetric arrangement in the spin channels (spin-up and spin-down). While the O 2p orbital split into the discrete level and intensity of localized Pt 3d states is significantly reduced, suggesting that the O_2 molecules are better activated.[57] Utilizing the free energy step diagram, the potential-determination-step (PDS) from OH_{abs} to H_2O in the ORR transversion on PtFe/FeN_4CCl is more prospective to enact than FeN_4C, FeN_4CCl and PtFe (**Figure 4h** and **Figure S24**). When the voltage is 1.23 V, the PDS of PtFe/FeN_4CCl-Pt site is the desorption of OH_{abs} ($OH_{abs} + H^+ + e^- \rightarrow H_2O_{abs}$). Obviously, the PtFe/$FeN_4$CCl-Pt site has a smaller Gibbs free energy change (ΔG_{pds}) (0.21 eV) relative to FeN_4C (0.75 eV), FeN_4CCl (0.37 eV), PtFe (0.88 eV), PtFe/FeN_4CCl-Fe site (0.71 eV), indicated that the synergistic effect of PtFe intermetallic and FeN_4CCl support enhances the catalytic efficiency and accelerates the ORR cycle. In addition, the DFT calculations were carried out to clarify the potential determination step (PDS) of the free energy step diagram on the ORR catalytic process based on electrochemical tests.[58] The DFT calculation results showed that the HOOH intermediates at Fe sites can release and migrate to the contiguous Pt sites for successive reactions, thereby effectuating integral oxygen reduction. (**Figure 4i** and **Figure S25**). [59,60] Such a result proved that the synergistic effect of between PtFe intermetallic and FeN_4CCl sites in the ORR process actualizes the four-electron transfer pathway.

To trace back the reason for the higher activity of PtFe/FeN_4CCl, the interaction between the catalytic site and OH_{abs} intermediate species was investigated. The bond length of Fe-OH in optimized models of FeN_4C, FeN_4CCl, PtFe/FeN_4CCl-Fe site is L_{Fe-OH}=1.82 Å, L_{Fe-OH}=1.86 Å, and L_{Fe-OH}=1.89 Å, individually. Identically, the bond length of Pt-OH of PtFe and PtFe/FeN_4CCl-Pt site is L_{Pt-OH}=1.96 Å and L_{Pt-OH}=2.27 Å, respectively, which reveals that activation O_2 molecule is easier to implement on the PtFe/FeN_4CCl-Pt active sites (**Figure 5a-c**). Synchronously, the adsorption free energy (E_{abs}) of OH_{abs} species on the Fe sites of FeN_4C, Fe sites of FeN_4CCl, Fe sites of PtFe/FeN_4CCl-Fe, Pt sites of PtFe, and Pt sites of PtFe/FeN_4CCl-Pt are E_{abs} = −3.07 eV, E_{abs} = −2.75 eV, E_{abs} = −3.12 eV, E_{abs} = −3.25 eV, and E_{abs} =−2.51 eV, respectively. Due to the axial-coordinated Cl atoms tugging more electrons deviated from the central metal atoms, the electronic circumstance was directly revised by orbital electron delocalization, which weakens the binding strength between the catalyst surface and the adsorbates. As shown in **Figure 5d**, the interaction between Fe $3dz^2$ orbitals and Cl 3pz orbitals contributes to strong dz^2-pz hybridization. The electron delocalization between the $3dz^2$ orbital in the FeN_4 moiety and the 2p orbitals of oxygen intermediates could turn the energy levels, splitting into bonding orbitals and antibonding states. The dz^2-state energy level of active site modified with axial-coordinated Cl atoms commonly down-shifts depart from the Fermi level.[61] Additionally, according to d-band theory, the alteration of the d-band center could affect its absorption capability of oxygen-containing intermediates.[62,63] Alloying Pt with a non-precious Fe element, which can exhibit a lattice contraction and a surface strain effect compared with pure Pt (**Figure 5c**). When oxygen-containing intermediates hybridize with a broader d band, the adsorbate state manufactures to split into localized bonding orbital and antibonding orbital.[64] The more electron occupancies of antibonding orbitals could downgrade the energy level of d-band center, thereby weakening the active sites adsorption energy. Besides, the PtFe intermetallic emanates the structurally ordered atomic arrangement and uniquely local geometrical properties, thus tremendously heightening higher ORR stability and activity.

3. Conclusions

In summary, a synergistic ORR catalyst with orbital electron delocalization axial-coordinated effect was successfully synthesized by utilizing hemin as a precursor on high-temperature pyrolysis. The unique structure of the as-prepared catalyst such as the ordered atomic arrangement and FeN_4CCl support with atomically dispersed Fe single-atoms was confirmed by the AC-HAADF-STEM images. XAFS analysis further demonstrates the existence of FeN_4Cl moiety with the Fe single-atom structure and the axial chlorine-coordinated coupling induction of FeN_4CCl substrate by configuring the Fe-N bond for ~1.92 Å and Fe-Cl bond for ~2.06 Å. More importantly, ELF and DFT further determine an orbital electron delocalization effect between Cl atoms and the FeN_4, resulting in electron redistribution and coordinated surroundings modification, thus optimizing the adsorption free energy of OH_{abs} intermediates for accelerating the electrocatalytic kinetics. Specifically, the obtained Pt_2Fe/FeN_4CCl catalyst with optimum surface composition displayed a higher catalytic performance, which was 9.92 times in MA, and 8.60 times in SA relative to commercial Pt/C catalyst, respectively. The LSV loss of $\Delta E_{1/2}$=16 mV after 40,000 cycles before and after an ADT, along with affording a marginal loss of 7.80 % in MA and 8.82 % in SA at a potential of 0.9 V vs. RHE, respectively. The heightened catalytic performance can be attributed not only to the orbital electron delocalization of axial-coordinated modified FeN_4CCl substrate, but also to the synergistic catalysis with the structurally ordered PtFe intermetallic. Our work manifests the crucial role of regulating the chemical environment of materials to optimize its electronic structure in catalysis and provides an alternative insight into designing synergistically efficient ORR catalysts.

4. Experimental section

Experimental procedures, material characterization, electrochemical measurement, and DFT computational details are listed in the Electronic Supplementary information.

Data availability

The authors declare that the data are available within the paper and its ESI file.

Author Contributions

Chenzhong Wu: Conceptualization, Investigation, Writing-original draft. Meida Chen: Data curation, Methodology Validation. Bin Wang: Data curation, Visualization. Leqing Luo: Data curation. Qian Zhou: Data curation. Guangtao Mao: Resources, Visualization. Yuan Xiong: Resources, Visualization. Qingmei Wang: Supervision, Writing-review & editing, Funding acquisition.

Conflicts of interest

The authors declare no conflict of interest.

Acknowledgements

This research work was financially supported by the National Natural Science Foundation of China (No. 22169005, 22068009 and 22262006), the Science and Technology Support Project of Guizhou Provincial Science and Technology Department (No. ZK[2023]050 and [2023]403), the Open Project of Institute of Dual-carbon and New Energy Technology Innovation and Development of Guizhou Province (No. DCRE-2023-06).

Notes and references

1 Tetteh, E. B.; Lee, H.-Y.; Shin, C.-H.; Kim, S.-h.; Ham, H. C.; Tran, T.-N.; Jang, J.-H.; Yoo, S. J.; Yu, J.-S., New PtMg Alloy with Durable Electrocatalytic Performance for Oxygen Reduction Reaction in Proton Exchange Membrane Fuel Cell. *ACS Energy Lett.* **2020**, 5 (5), 1601-1609.

2 Zhu, F.; Xu, K.; He, F.; Xu, Y.; Du, Z.; Zhang, H.; Zeng, D.; Liu, Y.; Wang, H.; Ding, D.; Zhou, Y.; Chen, Y., An Active and Contaminants-Tolerant High-Entropy Electrode for Ceramic Fuel Cells. *ACS Energy Lett.* **2024**, 9 (2), 556-567.

3 Wei, X.; Song, S.; Cai, W.; Kang, Y.; Fang, Q.; Ling, L.; Zhao, Y.; Wu, Z.; Song, X.; Xu, X.; Osman, S. M.; Song, W.; Asahi, T.; Yamauchi, Y.; Zhu, C., Pt Nanoparticle–Mn Single-Atom Pairs for Enhanced Oxygen Reduction. *ACS Nano* **2024**, 18 (5), 4308-4319.

4 Xiao, F.; Wang, Q.; Xu, G.-L.; Qin, X.; Hwang, I.; Sun, C.-J.; Liu, M.; Hua, W.; Wu, H.-w.; Zhu, S.; Li, J.-C.; Wang, J.-G.; Zhu, Y.; Wu, D.; Wei, Z.; Gu, M.; Amine, K.; Shao, M., Atomically dispersed Pt and Fe sites and Pt–Fe nanoparticles for durable proton exchange membrane fuel cells. *Nat. Catal.* **2022**, 5 (6), 503-512.

5 Chen, F., Chen, S., Wang, A., Wang, M., Guo, L., Wei, Z., Blocking the sulfonate group in Nafion to unlock platinum's activity in membrane electrode assemblies. *Nat. Catal.*, **2023**, *6*(5), 392-401.

6 Li, W.; Liu, B.; Liu, D.; Guo, P.; Liu, J.; Wang, R.; Guo, Y.; Tu, X.; Pan, H.; Sun, D.; Fang, F.; Wu, R., Alloying Co Species into Ordered and Interconnected Macroporous Carbon Polyhedra for Efficient Oxygen Reduction Reaction in Rechargeable Zinc–Air Batteries. *Adv. Mater.* **2022**, 34 (17), 2109605.

7 Xiong, P., Niu, H., Zhu, Z., Zhao, L., Zuo, J., Gong, S., Niu, X., Chen, J., Wu, R., and Xia, B., Engineering a High-Loading Sub-4 nm Intermetallic Platinum–Cobalt Alloy on Atomically Dispersed Cobalt–Nitrogen–Carbon for Efficient Oxygen Reduction in Fuel Cells. *Nano Lett.*, **2024**,24 (13), 3961-3970.

8 Wang, K.; Yang, H.; Wang, Q.; Yu, J.; He, Y.; Wang, Y.; Song, S.; Wang, Y., Electronic Enhancement Engineering by Atomic Fe – N_4 Sites for Highly - Efficient PEMFCs: Tailored Electric - Thermal Field on Pt Surface. *Adv. Energy Mater.* **2023**, 13 (14), 2204371.

9 Chen, M.; He, Y.; Spendelow, J. S.; Wu, G., Atomically Dispersed Metal Catalysts for Oxygen Reduction. *ACS Energy Lett.* **2019**, 4 (7), 1619-1633.

10 Yang, H.; Liu, Y.; Liu, X.; Wang, X.; Tian, H.; Waterhouse, G. I. N.; Kruger, P. E.; Telfer, S. G.; Ma, S., Large-scale synthesis of N-doped carbon capsules supporting atomically dispersed iron for efficient oxygen reduction reaction electrocatalysis. *eScience* **2022**, 2 (2), 227-234.

11 Yin, S.; Yan, Y.-N.; Chen, L.; Cheng, N.; Cheng, X.; Huang, R.; Huang, H.; Zhang, B.; Jiang, Y.-X.; Sun, S.-G., FeN_4 Active Sites Electronically Coupled with PtFe Alloys for Ultralow Pt Loading Hybrid Electrocatalysts in Proton Exchange Membrane Fuel Cells. *ACS Nano* **2023**, 18 (1), 551-559.

12 Qiao, Z.; Wang, C.; Zeng, Y.; Spendelow, J. S.; Wu, G., Advanced Nanocarbons for Enhanced Performance and Durability of Platinum Catalysts in Proton Exchange Membrane Fuel Cells. *Small* **2021**, 17 (48), 2006805.

13 Adabi, H.; Shakouri, A.; Ul Hassan, N.; Varcoe, J. R.; Zulevi, B.; Serov, A.; Regalbuto, J. R.; Mustain, W. E., High-performing commercial Fe–N–C cathode electrocatalyst for anion-exchange membrane fuel cells. *Nat. Energy* **2021**, 6 (8), 834-843.

14 Liu, M.; Sun, T.; Peng, T.; Wu, J.; Li, J.; Chen, S.; Zhang, L.; Li, S.; Zhang, J.; Sun, S., Fe-NC Single-Atom Catalyst with Hierarchical Porous Structure and P–O Bond Coordination for Oxygen Reduction. *ACS Energy Lett.* **2023**, 8 (11), 4531-4539.

15 Choi, C. H.; Lim, H.-K.; Chung, M. W.; Chon, G.; Ranjbar Sahraie, N.; Altin, A.; Sougrati, M.-T.; Stievano, L.; Oh, H. S.; Park, E. S.; Luo, F.; Strasser, P.; Dražić, G.; Mayrhofer, K. J. J.; Kim, H.; Jaouen, F., The Achilles' heel of iron-based catalysts during oxygen reduction in an acidic medium. *Energy Environ. Sci.* **2018**, 11 (11), 3176-3182.

16 Wang, Y., Huang, X., Wei, Z., Recent developments in the use of single-atom catalysts for water splitting. *Chin. J. Catal.*, **2021**, 42(8), 1269-1286.

17 Mei, Z.-y.; Cai, S.; Zhao, G.; Jing, Q.; Sheng, X.; Jiang, J.; Guo, H., Understanding electronic configurarions and coordination environment for enhanced ORR process and improved Zn-air battery performance. *Energy Storage Mater.* **2022**, 50, 12-20.

18 Yu, J.; Su, C.; Shang, L.; Zhang, T., Single-Atom-Based Oxygen Reduction Reaction Catalysts for Proton Exchange Membrane Fuel Cells: Progress and Perspective. *ACS Nano* **2023**, 17 (20), 19514-19525.

19 Chen, H., He, C., Niu, H., Xia, c., Li, F., Zhao, W., Song, F., Yao, T., Chen, Y., Su, Y., Guo, W., Xia, B., Surface Redox Chemistry Regulates the Reaction Microenvironment for Efficient Hydrogen Peroxide Generation. *J. Am. Chem. Soc.* **2024**, 146 (22), 15356-15365

20 Zeng, W.-J.; Wang, C.; Yan, Q.-Q.; Yin, P.; Tong, L.; Liang, H.-W., Phase diagrams guide synthesis of highly ordered intermetallic electrocatalysts: separating alloying and ordering stages. *Nat. Commun.* **2022**, 13 (1), 7654.

21 Guan, J.; Yang, S.; Liu, T.; Yu, Y.; Niu, J.; Zhang, Z.; Wang, F., Intermetallic FePt@PtBi Core–Shell Nanoparticles for Oxygen Reduction Electrocatalysis. *Angew. Chem. Int. Ed.* **2021**, 60 (40), 21899-21904.

22 Shi, Y.; Yang, W.; Gong, W.; Wang, X.; Zhou, Y.; Shen, X.; Wu, Y.; Di, J.; Zhang, D.; Li, Q., Interconnected surface-vacancy-rich PtFe nanowires for efficient oxygen reduction. *J. Mater. Chem. A* **2021**, 9 (21), 12845-12852.

23 Zou, X.; Chen, S.; Wang, Q.; Gao, X.; Li, J.; Li, J.; Li, L.; Ding, W.; Wei, Z., Leaching- and sintering-resistant hollow or structurally ordered intermetallic PtFe alloy catalysts for oxygen reduction reactions. *Nanoscale* **2019**, 11 (42), 20115-20122.

24 Chen, M.; Zhou, S.; Liao, W.; Wang, Z.; Long, J.; Zhou, Q.; Wang, Q., Ordered PtCo Intermetallics Featuring Nitrogen - Doped Carbon Prepared by Surface Coating Strategy for

Oxygen Reduction Reaction. *ChemElectroChem* **2022**, 9 (20), e202200803.
25 Wang, Q.; Tang, H.; Wang, M.; Guo, L.; Chen, S.; Wei, Z., Precisely tuning the electronic structure of a structurally ordered PtCoFe alloy via a dual-component promoter strategy for oxygen reduction. *Chem. Commun.* **2021**, 57 (33), 4047-4050.
26 Yoo, T. Y.; Lee, J.; Kim, S.; Her, M.; Kim, S.-Y.; Lee, Y.-H.; Shin, H.; Jeong, H.; Sinha, A. K.; Cho, S.-P.; Sung, Y.-E.; Hyeon, T., Scalable production of an intermetallic Pt–Co electrocatalyst for high-power proton-exchange-membrane fuel cells. *Energy Environ. Sci.* **2023**, 16 (3), 1146-1154.
27 Liu, B.; Feng, R.; Busch, M.; Wang, S.; Wu, H.; Liu, P.; Gu, J.; Bahadoran, A.; Matsumura, D.; Tsuji, T.; Zhang, D.; Song, F.; Liu, Q., Synergistic Hybrid Electrocatalysts of Platinum Alloy and Single-Atom Platinum for an Efficient and Durable Oxygen Reduction Reaction. *ACS Nano* **2022**, 16 (9), 14121-14133.
28 Cheng, Q.; Yang, S.; Fu, C.; Zou, L.; Zou, Z.; Jiang, Z.; Zhang, J.; Yang, H., High-loaded sub-6 nm Pt_1Co_1 intermetallic compounds with highly efficient performance expression in PEMFCs. *Energy Environ. Sci.* **2022**, 15 (1), 278-286.
29 Yang, J.; Hübner, R.; Zhang, J.; Wan, H.; Zheng, Y.; Wang, H.; Qi, H.; He, L.; Li, Y.; Dubale, A. A.; Sun, Y.; Liu, Y.; Peng, D.; Meng, Y.; Zheng, Z.; Rossmeisl, J.; Liu, W., A Robust PtNi Nanoframe/N‐Doped Graphene Aerogel Electrocatalyst with Both High Activity and Stability. *Angew. Chem. Int. Ed.* **2021**, 60 (17), 9590-9597.
30 Zhao, X.; Cheng, H.; Song, L.; Han, L.; Zhang, R.; Kwon, G.; Ma, L.; Ehrlich, S. N.; Frenkel, A. I.; Yang, J.; Sasaki, K.; Xin, H. L., Rhombohedral Ordered Intermetallic Nanocatalyst Boosts the Oxygen Reduction Reaction. *ACS Catal.* **2020**, 11 (1), 184-192.
31 Wang, N.; Mei, R.; Lin, X.; Chen, L.; Yang, T.; Liu, Q.; Chen, Z., Cascade Anchoring Strategy for Fabricating High-Loading Pt Single Atoms as Bifunctional Catalysts for Electrocatalytic Hydrogen Evolution and Oxygen Reduction Reactions. *ACS Appl. Mater. Interfaces* **2023**, 15 (24), 29195-29203.
32 Li, J.; Zhou, Q.; Yue, M.; Chen, S.; Deng, J.; Ping, X.; Li, Y.; Li, J.; Liao, Q.; Shao, M.; Wei, Z., Cross-linked multi-atom Pt catalyst for highly efficient oxygen reduction catalysis. *Appl. Catal. B Environ.* **2021**, 284, 119728.
33 Wang, X.; Fu, N.; Liu, J.-C.; Yu, K.; Li, Z.; Xu, Z.; Liang, X.; Zhu, P.; Ye, C.; Zhou, A.; Li, A.; Zheng, L.; Liu, L.-M.; Chen, C.; Wang, D.; Peng, Q.; Li, Y., Atomic Replacement of PtNi Nanoalloys within Zn-ZIF-8 for the Fabrication of a Multisite CO_2 Reduction Electrocatalyst. *J. Am. Chem. Soc.* **2022**, 144 (50), 23223-23229.
34 Chen, W.; Gao, W.; Tu, P.; Robert, T.; Ma, Y.; Shan, H.; Gu, X.; Shang, W.; Tao, P.; Song, C.; Deng, T.; Zhu, H.; Pan, X.; Yang, H.; Wu, J., Neighboring Pt Atom Sites in an Ultrathin FePt Nanosheet for the Efficient and Highly CO-Tolerant Oxygen Reduction Reaction. *Nano Lett.* **2018**, 18 (9), 5905-5912.
35 Ding, S.; Barr, J. A.; Shi, Q.; Zeng, Y.; Tieu, P.; Lyu, Z.; Fang, L.; Li, T.; Pan, X.; Beckman, S. P.; Du, D.; Lin, H.; Li, J.-C.; Wu, G.; Lin, Y., Engineering Atomic Single Metal–FeN4Cl Sites with Enhanced Oxygen-Reduction Activity for High-Performance Proton Exchange Membrane Fuel Cells. *ACS Nano* **2022**, 16 (9), 15165-15174.
36 Ao, X.; Zhang, W.; Zhao, B.; Ding, Y.; Nam, G.; Soule, L.; Abdelhafiz, A.; Wang, C.; Liu, M., Atomically dispersed Fe–N–C decorated with Pt-alloy core–shell nanoparticles for improved activity and durability towards oxygen reduction. *Energy Environ. Sci.* **2020**, 13 (9), 3032-3040.
37 Jiang, M.; Liu, W.; Yang, X.; Jiang, Z.; Yao, T.; Wei, S.; Peng, X., Pt/Fe_3O_4 Core/Shell Triangular Nanoprisms by Heteroepitaxy: Facet Selectivity at the Pt–Fe3O4 Interface and the Fe_3O_4 Outer Surface. *ACS Nano* **2015**, 9 (11), 10950-10960.
38 Chen, Y.; Li, Z.; Zhu, Y.; Sun, D.; Liu, X.; Xu, L.; Tang, Y., Atomic Fe Dispersed on N‐Doped Carbon Hollow Nanospheres for High‐Efficiency Electrocatalytic Oxygen Reduction. *Adv. Mater.* **2018**, 31 (8), 1806312.
39 Wan, X.; Liu, X.; Li, Y.; Yu, R.; Zheng, L.; Yan, W.; Wang, H.; Xu, M.; Shui, J., Fe–N–C electrocatalyst with dense active sites and efficient mass transport for high-performance proton exchange membrane fuel cells. *Nat. Catal.* **2019**, 2 (3), 259-268.
40 Xiao, F.; Xu, G.-L.; Sun, C.-J.; Hwang, I.; Xu, M.; Wu, H.-w.; Wei, Z.; Pan, X.; Amine, K.; Shao, M., Durable hybrid electrocatalysts for proton exchange membrane fuel cells. *Nano Energy* **2020**, 77, 105192.
41 Zitolo, A.; Goellner, V.; Armel, V.; Sougrati, M.-T.; Mineva, T.; Stievano, L.; Fonda, E.; Jaouen, F., Identification of catalytic sites for oxygen reduction in iron- and nitrogen-doped graphene materials. *Nat. Mater.* **2015**, 14 (9), 937-942.
42 Wan, X.; Liu, Q.; Liu, J.; Liu, S.; Liu, X.; Zheng, L.; Shang, J.; Yu, R.; Shui, J., Iron atom–cluster interactions increase activity and improve durability in Fe–N–C fuel cells. *Nat. Commun.* **2022**, 13 (1), 2963.
43 Rao, P.; Wu, D.; Wang, T.-J.; Li, J.; Deng, P.; Chen, Q.; Shen, Y.; Chen, Y.; Tian, X., Single atomic cobalt electrocatalyst for efficient oxygen reduction reaction. *eScience* 2022, 2 (4), 399-404.
44 Poerwoprajitno, A.; Gloag, L.; Watt, J.; Cheong, S.; Henson, A.; Subhash, B.; Bedford, N.; Miller, B.; O'Mara, P.; Benedetti, T.; Huber, D.; Gooding, J.; Schuhmann, W.; Tilley, R., A single-Pt-atom-on-Ru-nanoparticle electrocatalyst for CO-resilient methanol oxidation. *Nat. Catal.* **2022**, 5, 231-237.
45 van der Vliet, D. F.; Wang, C.; Li, D.; Paulikas, A. P.; Greeley, J.; Rankin, R. B.; Strmcnik, D.; Tripkovic, D.; Markovic, N. M.; Stamenkovic, V. R., Unique Electrochemical Adsorption Properties of Pt‐Skin Surfaces. *Angew. Chem. Int. Ed.* **2012**, 51 (13), 3139-3142.
46 Liu, J.; Jiao, M.; Lu, L.; Barkholtz, H. M.; Li, Y.; Wang, Y.; Jiang, L.; Wu, Z.; Liu, D.-j.; Zhuang, L.; Ma, C.; Zeng, J.; Zhang, B.; Su, D.; Song, P.; Xing, W.; Xu, W.; Wang, Y.; Jiang, Z.; Sun, G., High performance platinum single atom electrocatalyst for oxygen reduction reaction. *Nat. Commun.* **2017**, 8 (1), 15938.
47 Liao, W.; Zhou, S.; Wang, Z.; Long, J.; Chen, M.; Zhou, Q.; Wang, Q., Stress induced to shrink ZIF-8 derived hollow Fe-NC supports synergizes with Pt nanoparticles to promote oxygen reduction electrocatalysis. *J. Mater. Chem.* A **2022**, 10 (40), 21416-21421.
48 Sabhapathy, P.; Raghunath, P.; Sabbah, A.; Shown, I.; Bayikadi, K. S.; Xie, R.-K.; Krishnamoorthy, V.; Lin, M.-C.; Chen, K.-H.; Chen, L.-C., Axial Chlorine Induced Electron Delocalization in Atomically Dispersed FeN4 Electrocatalyst for Oxygen Reduction Reaction with Improved Hydrogen Peroxide Tolerance. *Small* **2023**, 19 (45), 2303598.
49 Shan, Y.; Zhang, X.; Liu, G.; Li, J.; Liu, Y.; Wang, J.; Chen, D., The Cyanations with Isocyanides: Recent Advances and Perspectives. *Chem. Commun.* **2024**, 60, 1546-1562.
50 Yang, H.; Ko, Y.; Lee, W.; Züttel, A.; Kim, W., Nitrogen-doped carbon black supported Pt–M (M = Pd, Fe, Ni) alloy catalysts for oxygen reduction reaction in proton exchange membrane fuel cell. *Mater. Today Energy* 2019, 13, 374-381.
51 Zhao, X.; Chen, J.; Bi, Z.; Chen, S.; Feng, L.; Zhou, X.; Zhang, H.; Zhou, Y.; Wågberg, T.; Hu, G., Electron Modulation and Morphology Engineering Jointly Accelerate Oxygen Reaction to Enhance Zn‐Air Battery Performance. *Adv. Sci.* **2023**, 10 (8), 2205889.
52 Sanville, E.; Kenny, S. D.; Smith, R.; Henkelman, G., Improved grid‐based algorithm for Bader charge allocation. Markovic, *Nat. Mater.* **2007**, 28 (5), 899-908.
53 Zhang, J.; Chen, J.; Luo, Y.; Chen, Y.; Luo, Y.; Zhang, C.; Xue, Y.; Liu, H.; Wang, G.; Wang, R., A defect-driven atomically dispersed Fe–N–C electrocatalyst for bifunctional oxygen

View Article Online
DOI: 10.1039/D4SC02824D

electrocatalytic activity in Zn–air batteries. *J. Mater. Chem. A* **2021**, 9 (9), 5556-5565.
54 Dai, Y.; Liu, B.; Zhang, Z.; Guo, P.; Liu, C.; Zhang, Y.; Zhao, L.; Wang, Z., Tailoring the d ‐ Orbital Splitting Manner of Single Atomic Sites for Enhanced Oxygen Reduction. *Adv. Mater.* **2023**, 35 (14), 2210757.
55 Jin, C., Li, J. Zhang, K. Habibullah, Xia, G., Wu, C., Wang, Y., Cen, W., Chen, Y., Yan, Y., Chen, Y., Pd_3P nanoparticles decorated P-doped graphene for high hydrogen storage capacity and stable hydrogen adsorption-desorption performance. *Nano Energy*, **2021**,*99*, 107360.
56 Dewar, M. J. S.; Thiel, W., Ground states of molecules. MNDO results for molecules containing hydrogen, carbon, nitrogen, and oxygen. *J. Am. Chem. Soc.* **1977**, 99 (15), 4907-4917.
57 Liu, K.; Fu, J.; Lin, Y.; Luo, T.; Ni, G.; Li, H.; Lin, Z.; Liu, M., Insights into the activity of single-atom Fe-N-C catalysts for oxygen reduction reaction. *Nat. Commun.* **2022**, 13 (1), 2075.
58 Venegas, R.; Recio, F. J.; Riquelme, J.; Neira, K.; Marco, J. F.; Ponce, I.; Zagal, J. H.; Tasca, F., Biomimetic reduction of O_2 in an acid medium on iron phthalocyanines axially coordinated to pyridine anchored on carbon nanotubes. *J. Mater. Chem. A* **2017**, 5 (24), 12054-12059.
59 Chong, L.; Wen, J.; Kubal, J.; Sen, F. G.; Zou, J.; Greeley, J.; Chan, M.; Barkholtz, H.; Ding, W.; Liu, D.-J., Ultralow-loading platinum-cobalt fuel cell catalysts derived from imidazolate frameworks. *Science* **2018**, 362 (6420), 1276-1281.
60 Huang, L., Su, Y. Q., Qi, R., Dang, D., Qin, Y., Xi, S., Zaman S., You, B., Ding, S., Xia, B., Boosting oxygen reduction via integrated construction and synergistic catalysis of porous platinum alloy and defective graphitic carbon. *Angew. Chem. Int. Ed.* **2021**, 60,25530–25537.
61 Hammer, B.; Nørskov, J. K., Electronic factors determining the reactivity of metal surfaces. Surf. Sci. **1995**, 343 (3), 211-220.
62 Cheng, Y.; Gong, X.; Tao, S.; Hu, L.; Zhu, W.; Wang, M.; Shi, J.; Liao, F.; Geng, H.; Shao, M., Mechano-thermal milling synthesis of atomically dispersed platinum with spin polarization induced by cobalt atoms towards enhanced oxygen reduction reaction. *Nano Energy* **2022**, 98, 107341.
63 Greiner, M. T.; Jones, T. E.; Beeg, S.; Zwiener, L.; Scherzer, M.; Girgsdies, F.; Piccinin, S.; Armbrüster, M.; Knop-Gericke, A.; Schlögl, R., Free-atom-liked states in single-atom alloy catalysts. *Nat. Chem.* **2018**, 10 (10), 1008-1015.
64 Wang, X.; Li, Y.; Wang, Y.; Zhang, H.; Jin, Z.; Yang, X.; Shi, Z.; Liang, L.; Wu, Z.; Jiang, Z.; Zhang, W.; Liu, C.; Xing, W.; Ge, J., Proton exchange membrane fuel cells powered with both CO and H_2. *Proc. Natl. Acad. Sci. U.S.A* **2021**, 118 (43), e2107332118.